Correlation between microstructure and intergranular corrosion behavior of low delta-ferrite content AISI 316L aged in the range 550–700 °C

A. Ben Rhouma [a], T. Amadou [a], H. Sidhom [a, *], C. Braham [b]

[a] Laboratoire de Mécanique, Matériaux et Procédés (LR99ES05), Université de Tunis, ENSIT, 5 AV Taha Hussein Montfleury, 1008 Tunis, Tunisia
[b] Laboratoire Procédés et Ingénierie en Mécanique et Matériaux (PIMM, CNRS UMR 8006), ENSAM, 151 Bd de l'Hôpital, 75013 Paris, France

Keywords:
Austenitic stainless steel
AISI 316L
ICG
Aging
Sensitization
Microstructure

A B S T R A C T

The microstructure and the phase identification of austenitic stainless steel AISI 316L with low δ-ferrite content (δ ≤ 1%) and aged for up to 80 000 h at temperatures ranging from 550 to 700 °C were investigated by using an optical microscope (OM), a scanning electron microscope (SEM) and a transmission electron microscope (TEM). Local changes of chromium content, resulting from nucleation and growth of chromium-rich phases during aging, were quantitatively assessed by energy dispersive X-ray spectroscopy (EDX) in the scanning transmission electron microscope (STEM). The intergranular corrosion behavior (IGC) of annealed and aged specimens was evaluated using the double loop electrochemical potentiokinetic reactivation (DL-EPR) and completed by IGC morphologies according to the ASTM A262 practice A standard.

The results showed that δ-ferrite decomposed gradually into $M_{23}C_6$ at 550 °C and decomposed totally into intermetallic phases (σ, η, χ, and R) and into secondary austenite (γ_r) at temperatures equal to or higher than 650 °C. Similarly γ-austenite decomposed into $M_{23}C_6$ carbide at 550 °C and into intermetallic phases such as η and σ in addition to carbide, at higher temperatures. The time-temperature-sensitization diagram (TTS) was established and used to calculate the critical cooling rate (CCR) that prevents IGC sensitization. The analysis of IGC results leads to the conclusion that sensitization-desensitization is still controlled by the characteristics of chromium-depleted area surrounding austenite grain boundary regions. No significant effect of remained δ-ferrite and derived components on the corrosion behavior of AISI 316 L containing 1% of δ-ferrite.

1. Introduction

Austenitic stainless steels are usually recommended for applications requiring high corrosion resistance materials. This property is due to the chromium content that is equal to or higher than 16 wt % that forms a self-healing protective film on the surface. However, these materials have modest low-temperature mechanical strength and they are recurred for high temperature application such as in nuclear power plants where they are used in sea water cooling pumps and steam generators. Moreover, these materials are currently used in more severe environments such as offshore platforms [1], food, chemical industries and medical application [2–5] due to their good toughness at a large temperature range [6] and to their resistance to pitting corrosion [4,7–9].

Despite the various attempts to enhance the corrosion resistance of these austenitic stainless steels [10–27], their susceptibility to hot cracking during cooling from welding [18,28] and their sensitivity to IGC during isothermal heating or continuous cooling after heating through the sensitization temperature ranging from 500 to 800 °C [16,20,29–33] remain unsolved. The state of the literature knowledge indicates that the convenient and commonly used method to prevent hot cracking consists in introducing a small amount of δ-ferrite in austenitic stainless steel [34–36]. It has been reported that a δ-ferrite fraction ranging from 1% to 6% is efficient to avoid hot cracking in the welded austenitic stainless steels. It also decreases the crack growth rate in SCC [34,35,37]. As for the susceptibility to intergranular corrosion, it was reported that after welding, cooling at a rate above the CCR prevents the sensitization to IGC. Therefore some values of CCR, depending on the microstructure and chemical composition, were provided [13]. Analysis

of literature data provided by various methods and tests [38–45] reveals the great influence of microstructure and chemical composition of austenitic steel on the IGC sensitivity and CCR. According to Sidhom et al. [44], the IGC sensitization was related to chromium-depleted areas resulting from $M_{23}C_6$ carbide precipitation during aging at temperatures ranging from 550 °C to 750 °C of the fully austenitic stainless steel type AISI 316L. Moreover, it was shown that the IGC sensitization-desensitization was controlled by the chromium level and by the width of the chromium depleted area. Similarly, Yae Kina et al. [27] studied the intergranular behavior of AISI 304 with low ferrite content during aging at 650 °C and 750 °C, and showed that δ-ferrite transformation to σ-phase does not occur for periods of up to 200 h. They attributed the sensitization phenomenon to $M_{23}C_6$ carbides and reported that the material has healed after 48 h at 750 °C but has not healed at 650 °C due to the thermally active bulk chromium diffusion process. Moreover, authors indicated that δ-ferrite remained stable during aging for periods of up to 200 h at 750 °C. However, Guanshun et al. [46] have shown that the δ-ferrite in Ti-modified super 304H decomposes rapidly into σ-phase, $M_{23}C_6$ carbides and secondary austenite during aging at 650 °C for periods of 4 h–500 h. These phases strongly influence the IGC resistance of the steel. They added that IGC sensitization at 650 °C of the studied material is associated basically with the σ-phase. In addition, they also established that higher fractions of δ-ferrite increase the IGC sensitization at 650 °C. Moreover, in the case of welded joints of austenitic stainless steels Garcia et al. [47] showed that the DOS of different welding zones has been correlated with the local changes in the material composition and its microstructure caused by the welding process. They showed that σ-phase, formed by the transformation of the δ-ferrite, contributed to the IGC sensitization of welded joints but less than the segregation phenomenon related to dendritic structure.

Despite the several studies devoted to the effect of small amounts of δ-ferrite on the IGC sensitization of austenitic stainless steel, some aspects are still unsolved:

- Even though the instability of δ-ferrite is evident, its decomposition process during heating and the associated quantitative depletion of chromium are still lacking for the comprehensive understanding of its effect on the corrosion behavior of austenitic stainless steel containing δ-ferrite.
- The decomposition of δ-ferrite has been often studied at relatively high temperatures such as 650 and 750 °C for relatively short aging periods of up to 500 h [27,46]. These conditions promote the σ-phase formation that generates less deep chromium depletion. Moreover, at this temperature range, the rapid bulk chromium diffusion enhances the healing process and IGC phenomena could then be concealed. Therefore, the conclusions related to the studied temperature range could not be valid for lower temperatures such as 600 and 550 °C and for very high aging durations due to other possible δ-ferrite decomposition mechanisms involving carbide precipitation.
- The effect of δ-ferrite transformation on the TTS diagram and the CCR has not yet been fully resolved due to the lack of a systematic study exploring a large range of sensitization temperatures.
- There is no predictive tool of IGC sensitization-desensitization to make extrapolation of DOS reliable for longer aging times at lower temperatures from short aging periods at higher temperature results.

To provide answers to the above raised issues, the microstructural evolution and the intergranular corrosion behavior of AISI 316L containing 1% of δ-ferrite during aging for periods varying from 50 h to 80 000 h at temperatures ranging from 550 to 700 °C are worth investigating. The 1% δ-ferrite content has been recommended by the nuclear boiler manufacturer, in order to avoid hot cracking and brittle sigma phase resulting from welding of austenitic stainless steel AISI 316L. It is therefore of considerable importance to identify the decomposition of ferrite and austenite during the aging process and to quantify the associated chromium depletion in order to understand their specific effects on the intergranular corrosion behavior. Secondly, the DOS corresponding to various aging conditions has been established using an electrochemical DL-EPR test, and correlated with the microstructural changes and with the chromium depletion area characteristics in order to deduce the IGC sensitization-desensitization criteria. Then, the TTS diagram was established and correlated with the TTP diagram in order to identify the role of phase decomposition on the IGC sensitization. The critical cooling rate avoiding IGC sensitization was calculated. Finally the effect of δ-ferrite on the intergranular corrosion behavior was discussed by superimposing TTS diagrams corresponding to stainless steels with different ferrite contents.

2. Material and aging conditions

The investigated material is an austenitic stainless steel type AISI 316L with a low carbon content C = 0.023 wt%. The chemical composition of the steel is given in Table 1. The test specimens were cut from a 30 mm thick hot-rolled plate. In the as received state, the samples underwent two annealing treatments by water quenching subsequent to holding at 1070 °C for 1 h. Aging treatments were carried out on the annealed samples at temperatures ranging from 550 to 700 °C for a short duration such as 50 h as well as for a very long duration of up to 80 000 h.

3. Tests and methods

3.1. Microstructure investigation techniques

The ferrite content of austenitic stainless steel was evaluated by measurements using Feritoscope type FMP 30. Microstructure investigations were carried out on the annealed and aged specimens before and after corrosion tests through using O. M, SEM and TEM. O. M and SEM examinations were conducted on samples polished using fine silicon carbide papers (180–2000 grades) then polished with 6 μm water-based diamond suspension and finally electrochemically polished in 10% oxalic acid solution in order to reveal the microstructure. The TEM observations were performed on thin foils with 3 mm diameter thinned by electro-polishing in a glycol ethylene solution cooled to 273 K (0 °C). Second phases formed during aging were identified by electron diffraction patterns carried

Table 1
Chemical composition of the AISI 316L (wt. %).

Elements	C	S	P	Si	Mn	Ni	Cr	Mo	Ti	Nb	Cu	N	B (ppm)
AISI 316L	0.023	0.008	0.029	0.4	1.7	12.1	17.4	2.44	<0.01	–	0.17	0.078	38

out on thin foils using an EM 430 Philips transmission electron microscope using 300 keV accelerating voltage. Their chemical composition was determined by EDX conducted on the carbon extractive replica in the STEM equipped with EDAX microanalysis hardware. Meanwhile, X-Ray microanalysis conducted on the thin foils was used to assess the evolution of chromium content of the depleted areas adjacent to γ/γ grain boundaries and in the δ-ferrite islands during aging.

3.2. Double loop electrochemical potentiokinetic reactivation tests and intergranular corrosion morphologies

The susceptibility to intergranular corrosion of the aged AISI 316L SS with low δ-ferrite content was evaluated using the double loop electrochemical potentiokinetic reactivation (DL-EPR) tests conducted in a conventional three-electrode cell. The working electrode was the sample which is cut in the rolling direction (RD) in order to evaluate the reactivity of the surface with a representative δ-ferrite content of the sheet (1%). The auxiliary and the reference electrodes were Pt and saturated calomel (SCE) respectively. Tests were carried out in an appropriate electrolyte consisting of 0.5 M H_2SO_4 + 0.01 M NH_4SCN at a temperature of 25 °C. The potential was varied from an active (- 400 mV/ECS) to a passive (+200 mV/ECS) domain with a scan rate equal to 1 mV/s. These test conditions were previously qualified as optimal to evaluate quantitatively the DOS of austenitic stainless steel grades [44,45]. The DOS was evaluated by the reactivation ratio (Ir/Ia%) where Ir is the reactivation (cathodic) current density peak and Ia is the activation (anodic) current density one. A ratio equal to or higher than 1% indicates that sensitization to IGC of the tested sample is confirmed by intergranular attacks (Fig. 1). The result of DL-EPR tests were completed by IGC morphology according to ASTM A262 (practice A) [38].

4. Results

4.1. Microstructural analysis

4.1.1. Annealed microstructure

The microstructure in the annealed state consists of islands of δ-ferrite aligned in the rolling direction of the sheet in an austenitic matrix with a grain size ranging from 70 to 100 μm. In the micrograph, the dark phase is that of the δ-ferrite whereas the bright one is that of the γ austenite (Fig. 2a). The volume fraction of δ-ferrite, assessed by the ferritoscope, was around 1%. The annealed microstructure is clearly free from intergranular γ/γ and δ/γ interface precipitations as shown in TEM micrographs (Fig. 2b and c).

4.1.2. Aged microstructure

SEM examinations of aged specimens reveal a rapid decomposition of δ-ferrite comparatively to γ austenite during aging at temperatures ranging from 550 to 700 °C. Indeed, SEM micrographs showed precipitates at the δ/γ interfaces while there was no visible precipitates at the γ/γ grain boundaries after aging at 550 °C for 1000 h (Fig. 3a). As aging at 550 °C continued from 1000 h to 10 000 h, precipitates grew substantially inside the δ-ferrite islands

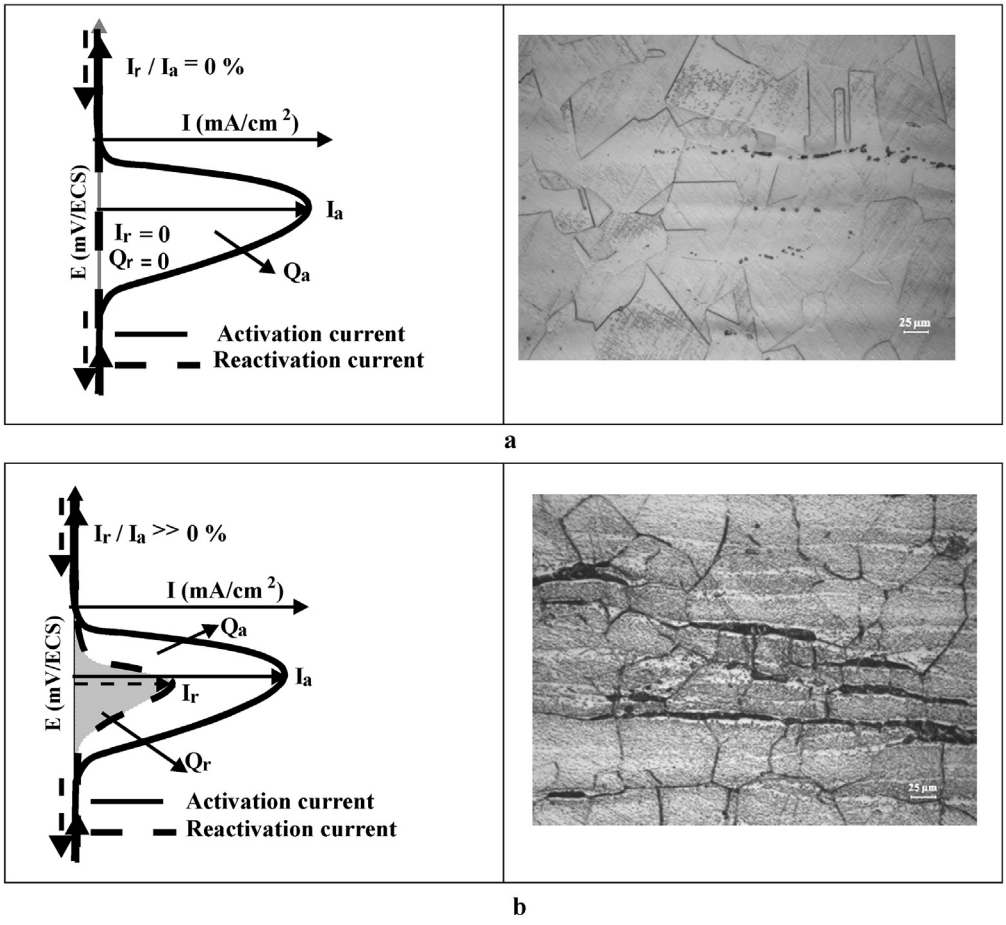

Fig. 1. DL-EPR responses and IGC sensitization criterion: (a) unsensitized material (I_r/I_a < 1%); (b) sensitized material ($I_r/I_a \geq$ 1%).

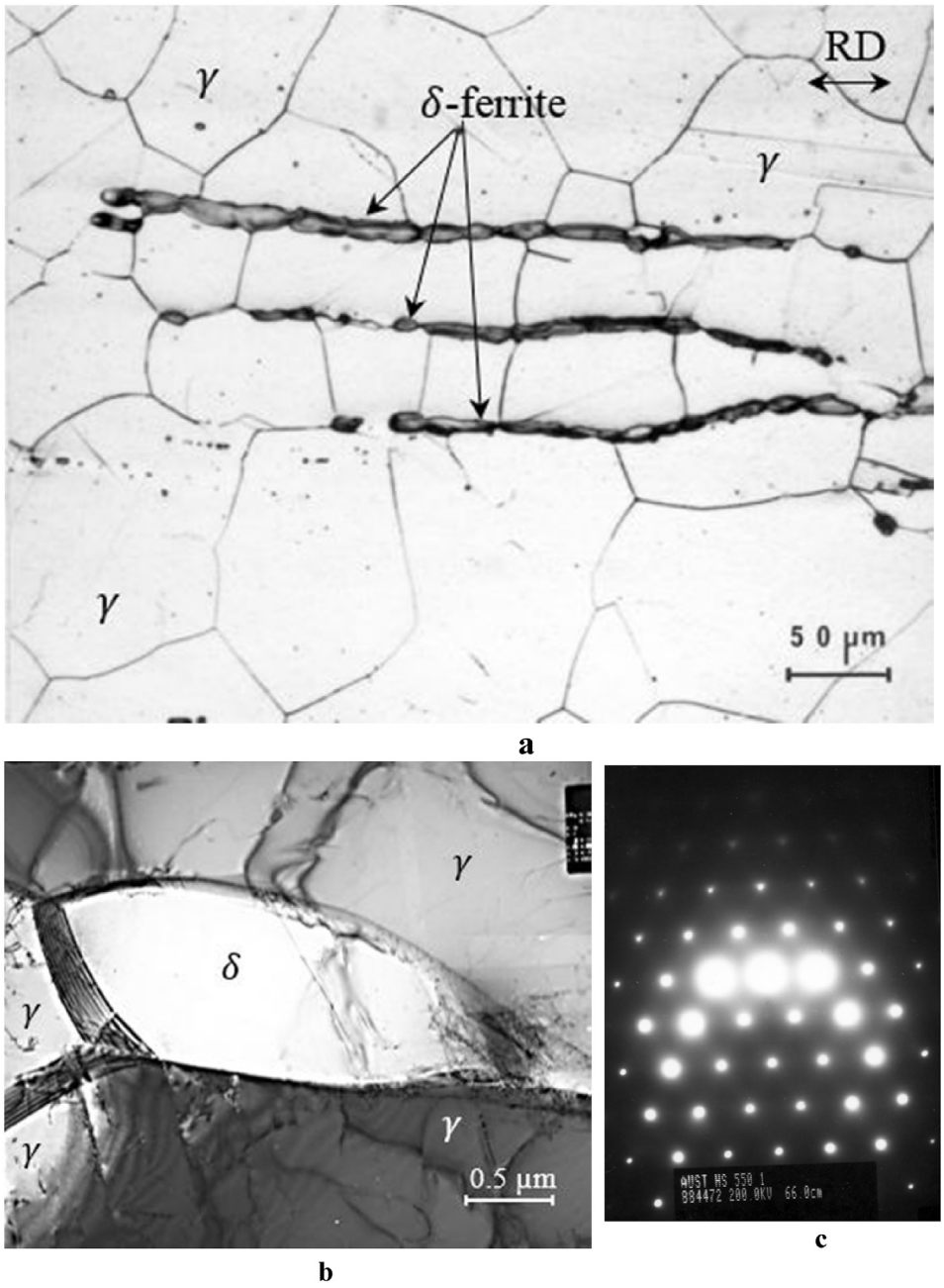

Fig. 2. Microstructure of annealed AISI 316 L: (a) Ferrite islands (optical micrograph); (b) δ ferrite grain (TEM micrograph); (c) SAD of ferrite, [111]δ.

whereas the first generative precipitate was observed at γ/γ grain boundaries (Fig. 3b). After higher aging duration such as 30 000 h, the typical eutectoid microstructure was observed inside the δ-ferrite islands (Fig. 3c) and the intergranular γ/γ precipitates encountered more austenite grains (Fig. 3d). Aging at higher temperatures, such as 600 and 650 °C, accelerates substantially the decomposition processes into δ and γ phases. Aging at 650 °C for 30 000 h leads to the total decomposition of δ-ferrite (Fig. 3e) and enhances the precipitates coarsening at the boundaries and inside austenite grains (Fig. 3f). These observations imply that the higher the aging temperature, the faster the decomposition of both ferrite and austenite phases due to the involved thermally active diffusion processes.

The TEM examination and the related selected area diffraction (SAD) have been used to identify the second phases formed during aging on the basis of crystalline structure analysis. The results summarized in Table 2 provide more information related to the effect of aging time and temperature on the microstructure evolution including precipitation sequences and sites. It can be inferred that the microstructural changes occurred easily in the δ/γ interfaces by the nucleation of a metastable intermetallic phase after a few hundred hours of aging at 550 °C (Fig. 4a and b). This phase was firstly assumed by Sidhom et al. [48] to be an icosahedral structure on the basis of typical SAD shown in Fig. 4b. Whilst, Carron et al. [49] have attributed this crystalline structure to the stacking faulted Frank Kaspar phases. After 1000 h at 550 °C, in addition to Frank Kaspar phases, $M_{23}C_6$ chromium carbides nucleated at the δ/γ interfaces and grew into δ ferrite (Fig. 4a and c). As the aging time increased to up 10 000 h at 550 °C, δ-ferrite was transformed gradually into $M_{23}C_6$ chromium carbides and into a

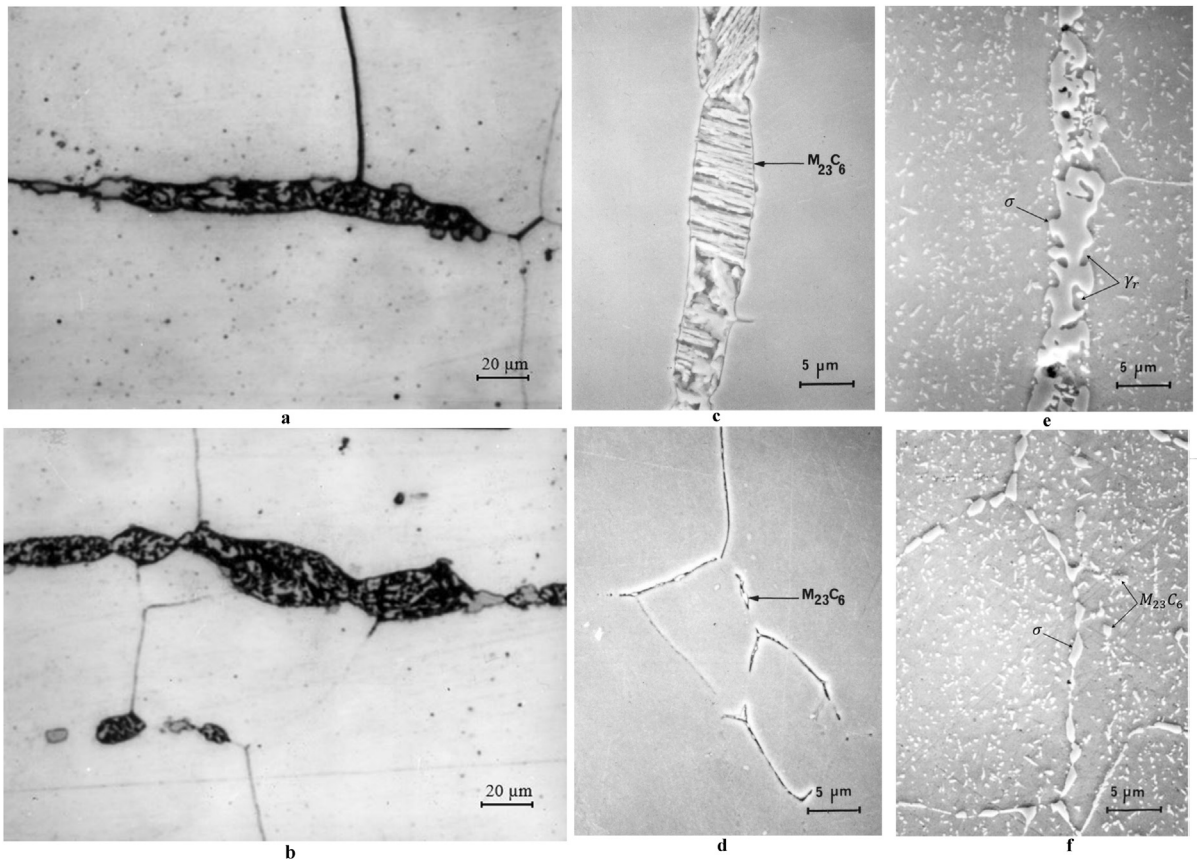

Fig. 3. Microstructure changes in austenite and ferrite during aging of AISI 316L (SEM examination): (a) Decomposition of δ ferrite after aging for 1 000 h at 550 °C; (b) Decomposition of δ ferrite after aging for 10 000 h at 550 °C; (c) Decomposition of δ ferrite after aging for 30 000 h at 550 °C; d) Precipitation of chromium carbide at the austenite grain boundaries after aging for 30 000 h at 550 °C; (e) Total transformation of δ ferrite after aging at 650 °C during 30 000 h; (f) Generalized precipitation in austenite after aging at 650 °C during 30 000 h.

Table 2
Carbides and intermetallic phases formed during aging of AISI 316L (TEM identification).

T (°C)	Sites of Precipitation	t (h)				
		100	1000	10 000	30 000	80 000
550	δ/γ	F.K phase	F.K phase, $M_{23}C_6$	$M_{23}C_6$	$M_{23}C_6$	$M_{23}C_6$
	δ		F.K phase, $M_{23}C_6$	$M_{23}C_6$, γ_r	$M_{23}C_6$, γ_r	$M_{23}C_6$, γ_r
	γ/γ	–	–	$M_{23}C_6$	$M_{23}C_6$	$M_{23}C_6$
	γ	–	–	$M_{23}C_6$	$M_{23}C_6$	$M_{23}C_6$
600	δ/γ	F.K phase, $M_{23}C_6$	$M_{23}C_6$	$M_{23}C_6$, η	$M_{23}C_6$, η, σ	n.e
	δ	$M_{23}C_6$	$M_{23}C_6$, γ_r	$M_{23}C_6$, γ_r	$M_{23}C_6$, γ_r,	n.e
	γ/γ	–	$M_{23}C_6$	$M_{23}C_6$, η	$M_{23}C_6$, η	n.e
	γ	–	$M_{23}C_6$	$M_{23}C_6$, η	$M_{23}C_6$, η	n.e
650	δ/γ	F.K phase, $M_{23}C_6$	$M_{23}C_6$, η	ð	ð	ð
				$M_{23}C_6$, η, σ, χ, R	$M_{23}C_6$, η, σ, χ, R	η, σ, χ, R
	δ	$M_{23}C_6$, γ_r	$M_{23}C_6$, γ_r	ð	ð	ð
				$M_{23}C_6$, γ_r, η,, σ, χ, R	γ_r, η, σ, χ, R	γ_r, η, σ, χ, R
	γ/γ	$M_{23}C_6$	$M_{23}C_6$, η	$M_{23}C_6$, η, σ	$M_{23}C_6$, η, σ, χ	η, σ, χ
	γ	–	$M_{23}C_6$, η	$M_{23}C_6$, η	$M_{23}C_6$, η, σ, χ	$M_{23}C_6$, η, σ, χ
700	δ/γ	$M_{23}C_6$	σ, γ_r	ð	n.e	n.e
	δ	$M_{23}C_6$, γ_r	σ, γ_r	ð	n.e	n.e
	γ/γ	$M_{23}C_6$, η	$M_{23}C_6$, η, σ	$M_{23}C_6$, η, σ	n.e	n.e
	γ	$M_{23}C_6$	$M_{23}C_6$, η	$M_{23}C_6$, η, σ	n.e	n.e

-: no precipitate.
n.e: no examined.
F.K: Frank Kaspar phase.
η: Laves phase.
γ_r: Regenered austenite.
ð: Total decomposition of δ ferrite.

regenerated austenite (γ_r) (Fig. 5a and b), while a small number of carbides appeared at the γ/γ grain boundaries (Fig. 5c). There was no other second phase formed until 80 000 h at 550 °C, while the carbides coarsened substantially into δ-ferrite (Fig. 6a) at the γ/γ grain boundaries and in the dislocation pull ups into γ grains (Fig. 6b). However, it is important to notice that, at 550 °C, when the aging time is extended, the Frank Kaspar phase disappears in favor of $M_{23}C_6$ carbides and the δ-ferrite is not totally transformed after aging for up to 80 000 h.

Aging at a higher temperature such as 650 °C promotes the precipitation of various intermetallic phases in addition to $M_{23}C_6$ carbides. The precipitation sequences occurred firstly at the δ/γ

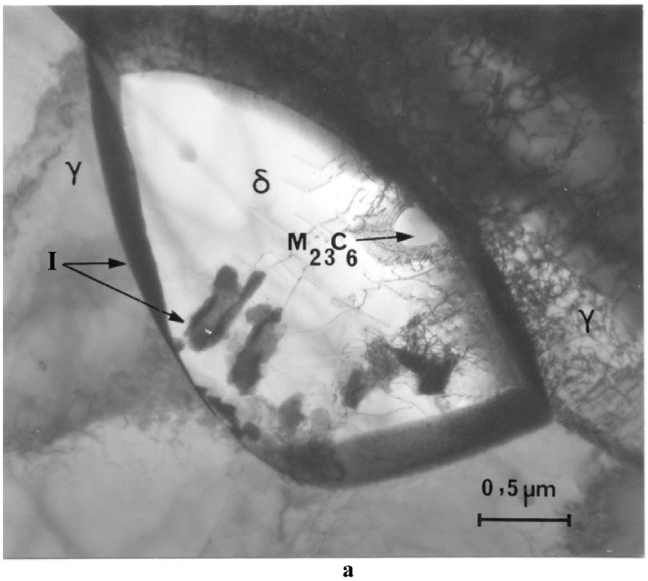

a

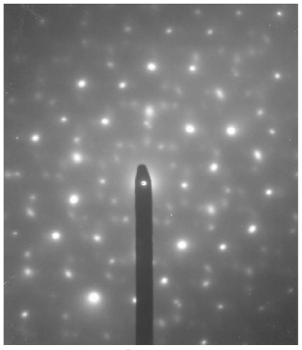

b

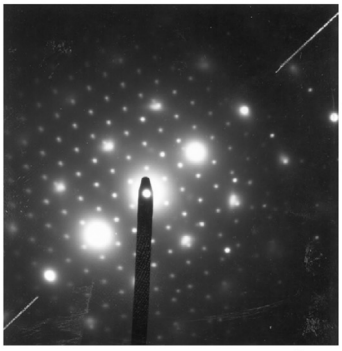

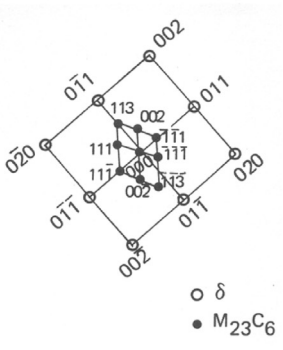

c

Fig. 4. Decomposition of δ ferrite after aging at 550 °C during 1000 h (TEM examination): (a) F.K phase (I phase) and $M_{23}C_6$ carbide at the δ/γ interface; (b) SAD of F.K phase and δ ferrite matrix; (c) SAD of $M_{23}C_6$ carbide and δ ferrite matrix.

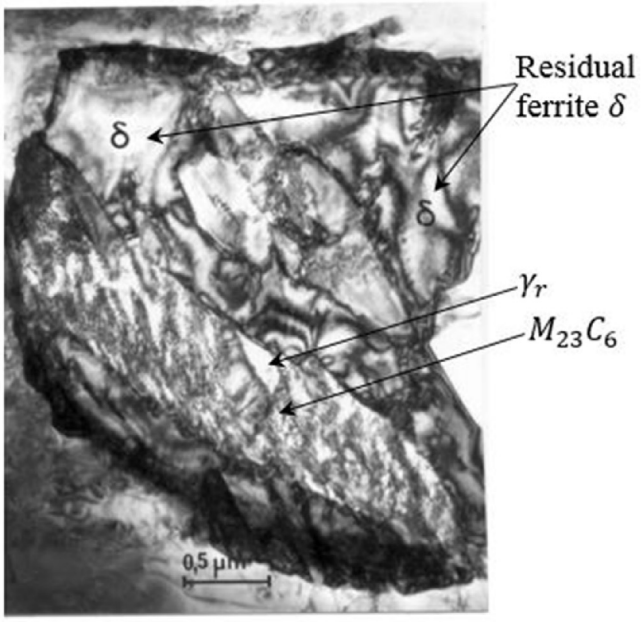

a

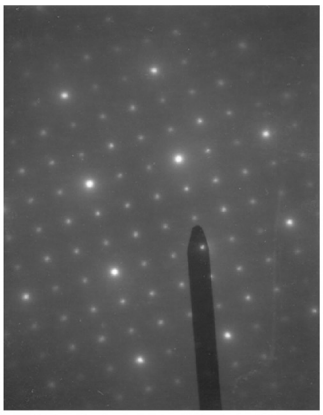

b

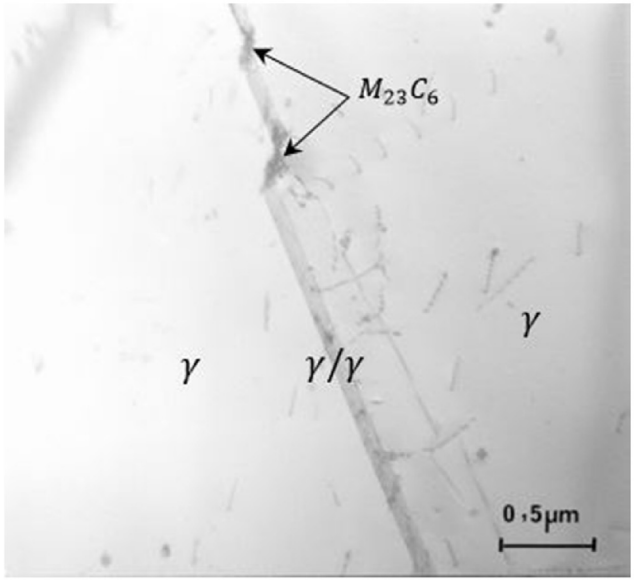

c

Fig. 5. Decomposition of δ ferrite after aging at 550 °C during 10 000 h (TEM examination): (a) Decomposition of δ ferrite into $M_{23}C_6$ and regenered austenite (γ_r); (b) SAD of $M_{23}C_6$ carbide and regenered austenite (γ_r); (c) Nucleation of $M_{23}C_6$ carbide at the austenite grain boundaries.

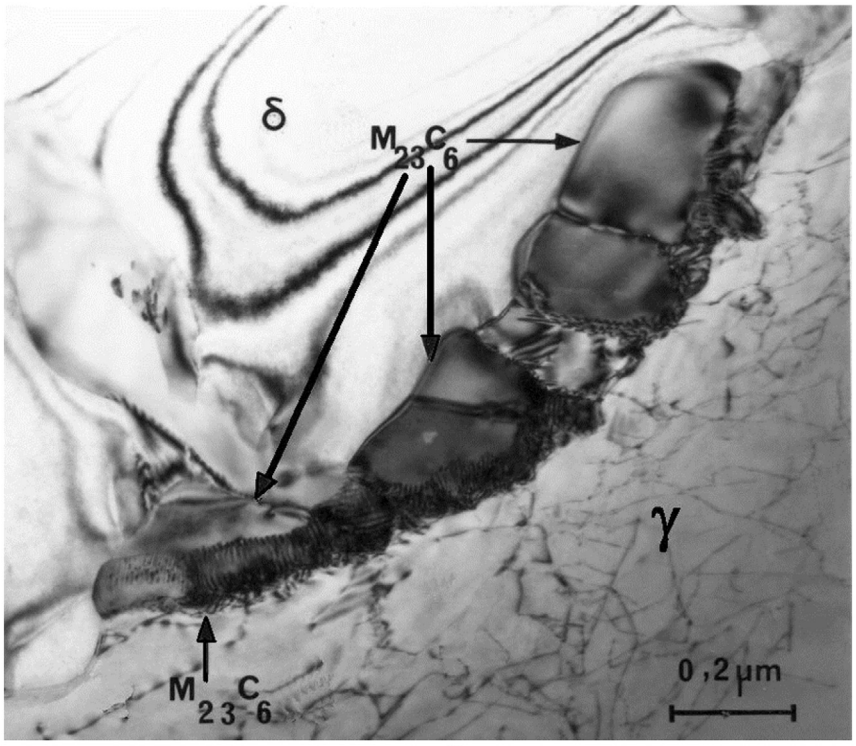

a

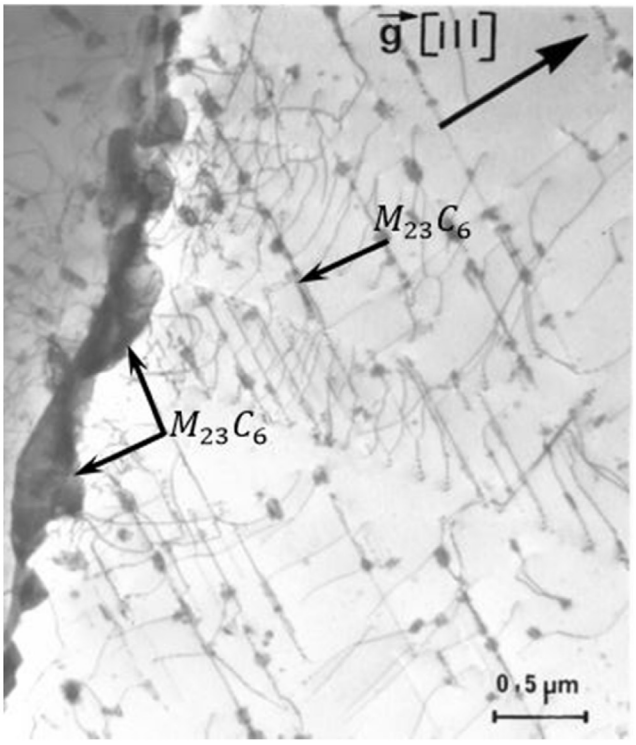

b

Fig. 6. Nucleation and growth of $M_{23}C_6$ carbide after aging at 550 °C during 80 000 h: (a) Coarsing of $M_{23}C_6$ carbide at γ/δ interface; (b) Nucleation of intragranular $M_{23}C_6$ on the dislocation pull ups.

interfaces and later at γ/γ grain boundaries and inside the austenite grains. Therefore, the δ-ferrite domain gradually becomes smaller due to the decomposition process and eventually disappears completely after 10 000 h at 650 °C to the benefit of intermetallic phases σ, χ, η (Laves phase), R and regenerated austenite γ_r (Fig. 7a). The SAD related to each phase was reported in Fig. 7 b, c, d and e. The second austenite phase γ_r formed initially at the δ/γ interfaces grew along the austenite phase edge. This phase is therefore not easily distinguishable from the annealed austenite. The χ, η and R phases appeared systematically with the σ-phase

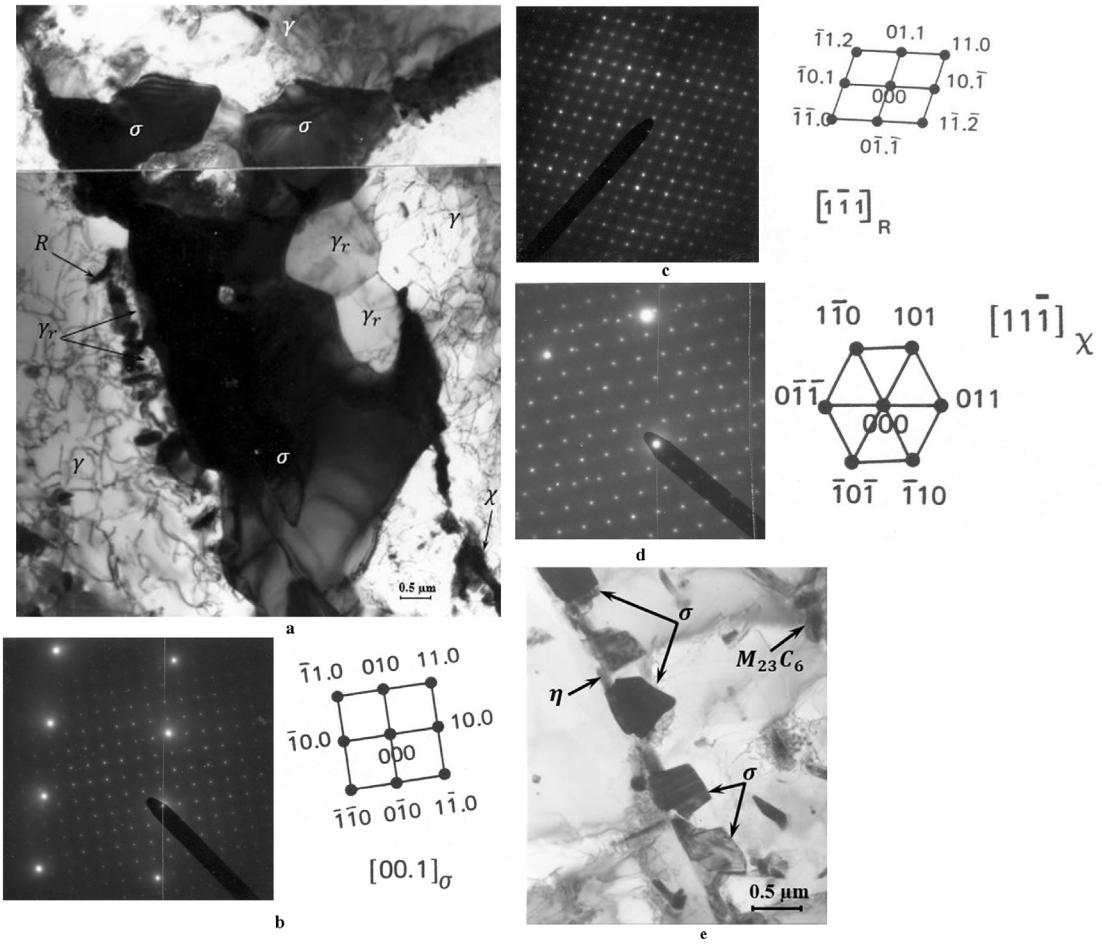

Fig. 7. Precipitation of intermetallic phases after aging at 650 °C during 10 000 h: (a) Total decomposition of δ ferrite into γ_r, χ, R and σ phases; (b) SAD of σ phase and austenite matrix; (c) SAD of R phase; (d) SAD of χ phase and austenite matrix; (e) Nucleation and growth of σ phase at the austenite grain boundaries.

although it seems that they precipitated prior to σ-phase because of the required higher interface energy. Moreover, σ-phase was larger than the other intermetallic phases and its volume fraction increased with increasing aging time and temperature. Otherwise, the absence of carbides, as a δ decomposition product, suggests that these carbides are completely dissolved in favor of σ-phase which evolves substantially into ferrite. Because of the complete decomposition of the δ-phase, there was no significant microstructural changes related to the ferrite islands after extending the aging periods to up to 30 000 h at 650 °C. However, carbides, η and σ phases nucleated at the γ/γ grain boundaries grew by increasing aging time (Fig. 7e).

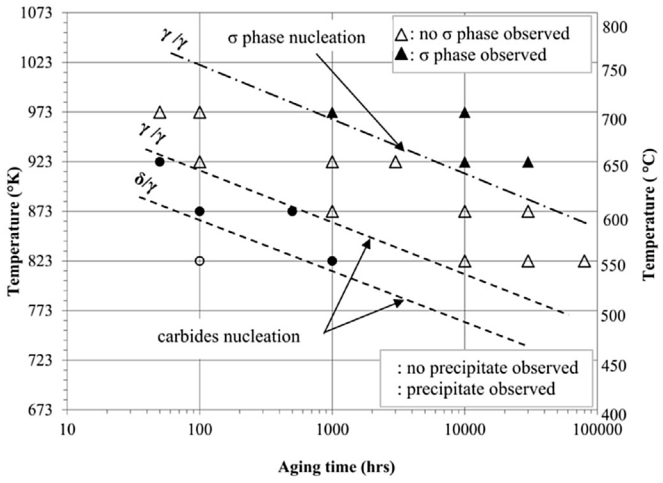

Fig. 8. TTP diagram of AISI 316 L with low ferrite content using TEM examination results.

The results of TEM examinations, reported in Table 2, were used to construct the TTP diagram by plotting the time and temperature of the second phase nucleation in each parent phase (δ and γ). This diagram showed that the microstructure instability of the annealed AISI 316 L underwent decomposition during aging at temperatures ranging from 550 to 700 °C (Fig. 8). According to the experimental results, the transformation mechanisms of the parent phases δ and γ that depend basically on the aging time and temperature could be described as follows:

$$\delta \rightarrow \text{(F.K) phases} + M_{23}C_6 \rightarrow M_{23}C_6 + \gamma_r \rightarrow \gamma_r + \eta + \chi + R + \sigma$$

$$\gamma \rightarrow \gamma + M_{23}C_6 + \eta + \sigma$$

4.1.3. Chromium-rich phases

Precipitates identification was completed by quantitative analysis of their chemical composition which is carried out on an extractive replica in STEM. Results reported in Table 3 confirm that carbides were chromium rich phase (71 wt %). The intermetallic

Table 3
Chemical composition of carbide and intermetallic phases formed during aging of AISI 316L (EDS analysis in STEM).

Aging conditions		Phases	Elements content (wt. %)					
Temperature (°C)	Duration (h)		Si	Cr	Mn	Fe	Ni	Mo
550	100	F.K phase	3.0	30.0	1.3	28.3	4.1	33.3
550	80 000	$M_{23}C_6$	0.2	71.2	1.6	16.8	2.4	7.8
650	10 000	Laves phase η	3.5	33.0	1.4	27.6	4.5	30.0
650	10 000	χ	1.4	25.0	2.5	50.0	3.0	18.1
650	10 000	R	1.5	20.0	1.0	47.3	3.5	27
650	10 000	σ	0.8	35.8	2	50	2.7	8.7
650	10 000	γ_r	0.3	16	1.6	74.1	7.2	0,8

compounds such as F.K, η, χ, R and σ were chromium and molybdenum rich phases. These results also show that the chromium content of the secondary austenite (γ_r) (14–16 wt %) resulting from the δ-ferrite decomposition, is slightly lower than that of the initial austenite (17.4 wt %). The chromium enrichment of the precipitates results in the depletion of the neighboring regions, as illustrated qualitatively by chromium mapping provided by STEM X-ray image using chromium Kα radiation (Fig. 9). Mapping showing brightness contrast is related to different Cr-enrichment. The brightest zone corresponds to Cr-enriched $M_{23}C_6$ carbide formed during aging at the δ/γ interfaces (Fig. 9a) and at the γ/γ grain boundaries (Fig. 9b). It is also shown that the carbide chromium enrichment was made at the expense of the surrounding ferrite and austenite grain boundary regions.

4.1.4. Chromium depleted area

As shown in Fig. 9, the nucleation and growth of chromium-rich phases and mainly $M_{23}C_6$ carbides, impact chromium content and increase the chromium depleted zones in the vicinity of the γ/γ grain boundaries, the δ/γ interfaces and inside the remained δ-ferrite. The chromium profiles, established by EDX microanalysis in STEM, provide quantitative evolution of the chromium concentration and the extent of the depleted zones which are related to the intergranular (γ/γ) precipitation of chromium-rich phases which depends mainly on the aging duration and temperature (Fig. 10). It can be inferred that chromium level at the γ/γ grain boundaries (and also at the γ/$M_{23}C_6$ interphase) falls below 12 wt % (13 at %) during aging at 550 °C for durations between 10 000 h and 80 000 h and that the chromium depleted area width increased from 40 nm to 200 nm (Fig. 10a). During aging at 600 °C, the chromium content at the γ/γ grain boundaries falls below 12 % wt after a period of 1000 h and recovers gradually its initial level after a duration higher than 30 000 h (Fig. 10b). At a temperature of 650 °C, the rechromisation phenomenon was fast enough for the γ/γ chromium level (16.5 wt %) to almost fully recover when the aging time reaches 10 000 h (Fig. 10c).

Similarly, the δ-ferrite chromium concentration decreased significantly during aging as a consequence of carbides and intermetallic phase precipitation (Fig. 11). The minimum chromium content ranging from 8 wt % to 10 wt % was reached at 550 °C for aging durations ranging from 10 000 h to 80 000 h. At higher temperatures, chromium decreased rapidly below 8 wt % before complete decomposition of δ-ferrite which occurred after 30 000 h at 600 °C, 10 000 h at 650 °C and only 100 h at 700 °C. Therefore 14 to 16 wt % chromium content was measured in secondary austenite (γ_r).

4.2. Intergranular corrosion behavior

4.2.1. Time-temperature-sensitization diagram

The experimental values of the ratio Ir/Ia (%), resulting from the DL-EPR tests conducted on the annealed and aged specimens are listed in Table 4. Ir/Ia, considered as an indicator of the DOS, evolved from 0% (unsensitized state) to 38.4% (very sensitized state). The sensitization at 550 °C occurred after 10 000 h and continued beyond 80 000 h. At higher temperatures, the sensitization is rapid and followed by the desensitization, which is marked by the drop of the Ir/Ia ratio to 0%. This desensitization occurs after aging for

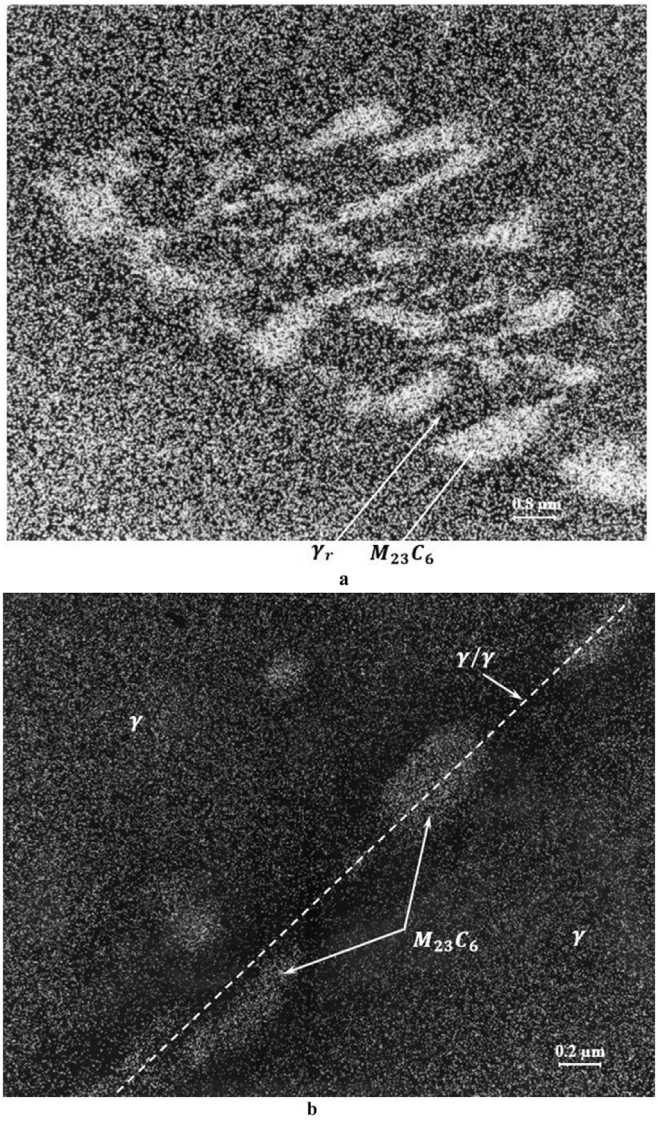

Fig. 9. Chromium depleted area resulting from nucleation and growth of $M_{23}C_6$ rich-chromium carbide after aging at 600 °C during 10 000 h (STEM micrographs); (a) Kα chromium mapping into δ ferrite; (b) Kα chromium mapping of austenite grain boundarie region.

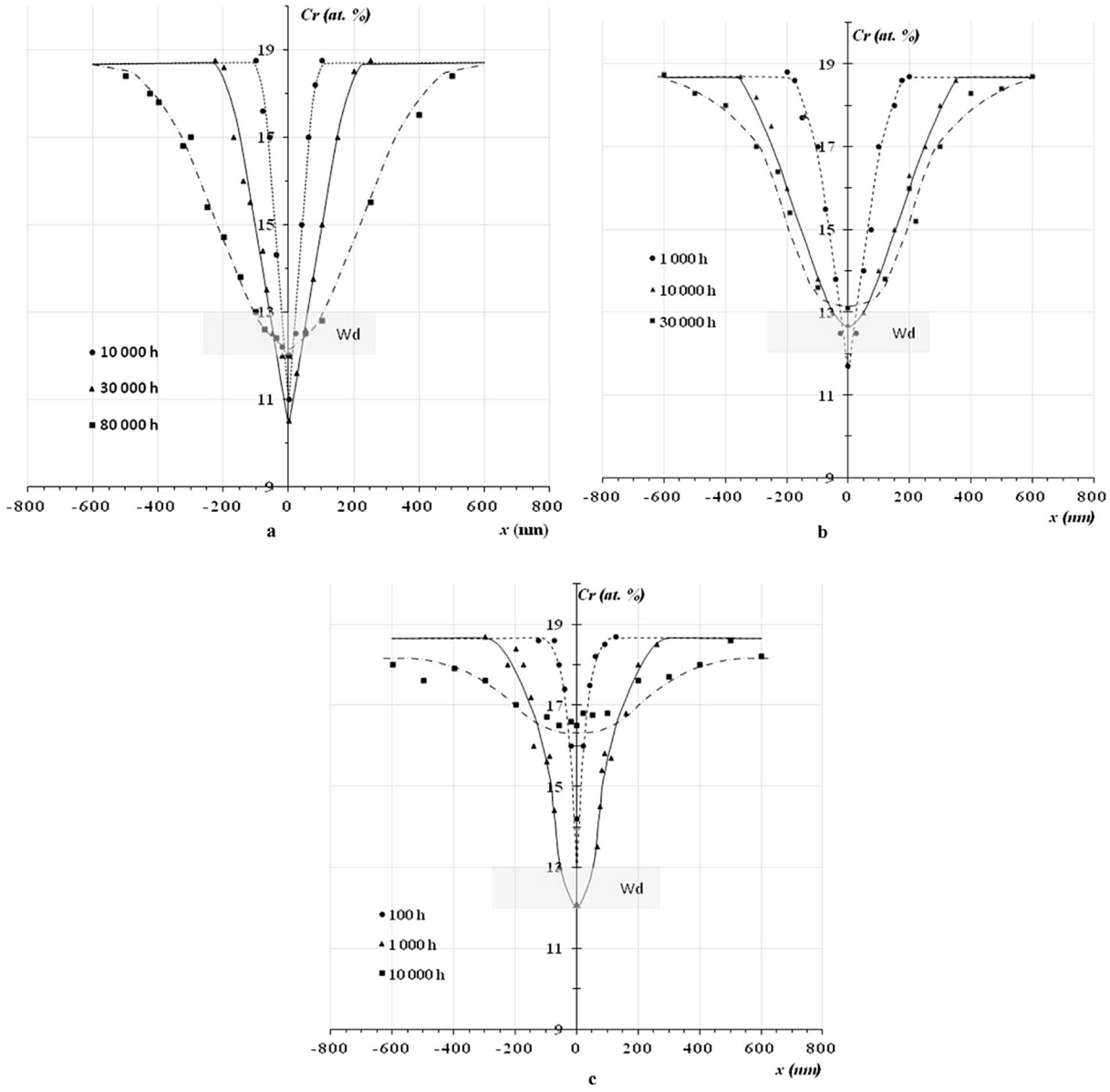

Fig. 10. Evolution of chromium concentration at the vicinity of austenitic grain boundary during aging of AISI 316 L; (a) T = 550 °C; (b) T = 600 °C; (c) T = 650 °C.

periods longer than 30 000 h at 600 °C, 10 000 h at 650 °C and 1000 h at 700 °C. Using the sensitization criteria Ir/Ia ≥1%, the TTS diagram was established (Fig. 12 a). It can be inferred that aging at temperatures ranging from 550 to 700 °C sensitized the low ferrite content austenitic stainless steel to IGC. At the peak temperature which is around 730 °C, the time required for sensitization is about 50 h while it is higher than 8000 h at 550 °C. The sensitization period ($\Delta t = t_f - t_s$) defined as the difference between the sensitization finishing time (t_f) and the sensitization starting time (t_s) varies between 650 h at 700 °C and 200 000 h at 550 °C. It is important to notice that, in industrial practice, the TTS diagram can be directly used for controlling the risk of IGC sensitization under isothermal heating. In order to avoid the sensitization resulting from continuous cooling through the sensitization temperature range, the cooling rate must be above a critical value. This value is different from that provided by the intersection of superimposed cooling curve and the isothermal TTS diagram as $\frac{\Delta T_{500}^{700}}{\Delta t_{500}^{700}} = 220^{\pm 20}\,°C/h$. This difference is the result of not taking into account the effect of time spent at the different temperature levels during cooling. Therefore, Dayal et al. [13] proposed a new method to calculate, from TTS diagram, the CCR which is of great interest to predict whether the cooling of heated or welded structure was sensitized or not. According to Dayal et al., the CCR is given by equation (1):

$$CCR = \Delta T \sum_{T_L}^{T_H} \frac{1}{t_s} \tag{1}$$

Where T_H is the highest temperature, T_L is the lowest temperature, ts is the sensitization time and ΔT is the temperature difference in the considered small temperature steps.

The calculated CCR value is 24 K/h for AISI 316L with 1% δ-ferrite. Otherwise, from the superimposition of TTP and TTS diagrams in

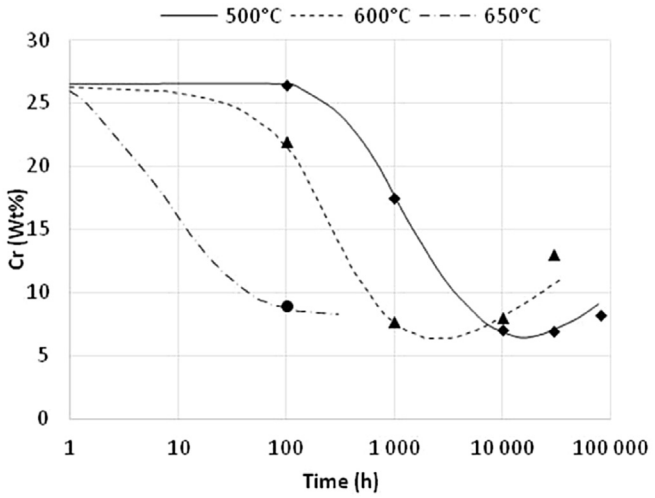

Fig. 11. Evolution δ ferrite chromium content during aging of AISI 316 L.

selected 1/T (K)-Ln (t) axis (Fig. 12 b) it can be seen that:

- The IGC sensitization is considered to be the consequence of $M_{23}C_6$ carbide nucleation and growth, while it seems to be independent of σ-phase precipitation which occurs at higher temperature and longer aging duration corresponding to desensitization region;
- The chromium-rich carbide precipitation and subsequent sensitization and desensitization phenomena are thermally activated processes. Assuming that the processes follow an Arrhenuis rate equation, the time to IGC sensitization can be written as follows:

$$t = C.exp\left(-\frac{Q}{RT}\right) \tag{2}$$

Where C is a constant, $R = 8.314\,J.mol^{-1}.K^{-1}$, Q ($J.mol^{-1}$) is the activation energy and T is the absolute temperature in Kelvin.

The activation energy which is valid at temperatures ranging between 550 °C and 700 °C was assessed to be 260 ± 14 $KJ.mole^{-1}$ corresponding to the Chromium diffusion process in austenitic steels as reported in the literature [14]. Therefore, an equivalent time–temperature relationship can be used to predict the duration of equivalent DOS resulting from other aging temperatures, using the following equation:

$$\frac{t1}{t2} = \exp\left(-\frac{Q}{R}\left(\frac{1}{T1} - \frac{1}{T2}\right)\right) \tag{3}$$

Where t_1 is aging duration at temperature T_1, t_2 is aging duration at temperature T_2, R is ideal gas constant and Q is apparent activation energy.

Using this equation, it is easy to verify that the DOS of samples aged for 10 000 h at 550 °C is similar to that of samples aged for 1000 h at 600 °C.

4.2.2. Intergranular corrosion morphologies

The IGC morphologies observed after etching according to the ASTM A262 practice A standard, for various aging conditions revealed globally an attacked structure "closely" correlated with the DOS determined by the Ir/Ia ratio. It is clear that the higher the DOS the wider the corrosion attack at the γ/γ grain boundaries, which indicates a selective dissolution of chromium depleted area (Fig. 13). As expected, the annealed specimen which is declared unsensitized by the DL-EPR test (DOS = 0%) did not show any IGC attack and consequently, it is classified as "step structure", according to the ASTM A262 practice A standard [38] (Fig. 13a, d and 13g). However, the specimens aged at 550 °C showed evident attack at the γ/γ grain boundaries, a slight attack at the δ/γ interface and a local attack inside δ. These attacks increased with increasing aging time as evidenced by the DOS evolving from 2.5% for a 10 000 h aging period (Fig. 13b) to 38.4% for an 80 000 h aging period (Fig. 13c). For 10 000 h aging period, attack structure were classified as "dual structure", meanwhile for 80 000 h aging period the attack structure was considered as "ditch structure" since numerous grains were completely encircled by attack. Similar morphologies (dual) were observed at higher temperatures but for shorter aging periods such as 1000 h at 600 °C (Fig. 13e) and 100 h at 650 °C (Fig. 13h). Longer periods at these temperatures showed ditch structure (Fig. 13f and i). Based on the above observations, the DL-EPR test results are correlated with the results of tests conducted according to the ASTM A262 practice A and therefore, the criterion of sensitization starting Ir/Ia ≥ 1% is realistic since it is well validated by the IGC morphologies shown in Fig. 13. It is important to notice

Table 4
DOS values resulting from DL-EPR tests carried out on the aged AISI 316L specimens.

Aging conditions		Degree of sensitization					
Temperature (°C)	Duration (h)	I_a (mA/cm^2)	I_r (mA/cm^2)	I_r/I_a (%)	Q_a (μC/cm^2)	Q_r (μC/cm^2)	Q_r/Q_a (%)
1100	1	1.79	0.0	0.0	107.66	0.0	0.0
550	1000	2.29	0.0	0.0	150.15	0.0	0.0
	10 000	5.25	0.13	2.5	429.22	39.15	9.1
	30 000	11.06	0.8	7.2	1054.6	178.3	16.9
	80 000	11.16	4.28	38.4	1093.8	550.5	50.3
600	500	2.14	0.0	0.0	135.12	0.0	0.0
	1000	9.24	0.23	2.5	752.18	27.48	3.7
	10 000	9.45	1.64	17.4	781.24	167.2	21.4
	30 000	20.13	0.51	2.5	1990.5	50.44	2.5
650	50	2.05	0.0	0.0	131.12	0.0	0.0
	100	8.83	0.24	2.8	736.76	26.22	3.6
	1000	9.87	3.29	33.3	910.27	291.5	32.0
	10 000	26.15	0.0	0.0	2369.2	0.0	0.0
	30 000	40.04	0.0	0.0	3832.0	0.0	0.0
700	50	3.35	0.20	2.6	1391.9	43.15	3.1
	100	4.54	0.77	17.0	375.75	81.89	21.79
	1000	15.43	0.0	0.0	1357.7	0.0	0.0
	10 000	29.62	0.0	0.0	2604.7	0.0	0.0

that the attack on the δ/γ interface was rarely observed, even after a total decomposition of δ-ferrite into σ-phase. This suggests that there is no detrimental effect of the 1% wt of the δ-ferrite on the IGC resistance of austenitic stainless steel. However some pits resulting from δ-ferrite decomposition were observed in the vicinity of σ-phase (Fig. 14).

4.3. Microstructure-intergranular corrosion sensitization/desensitization relationship

The correlation between microstructure and DL-EPR results completed by the IGC morphologies is evidenced by data reported in Table 5. It gives a great importance to chromium-depleted areas

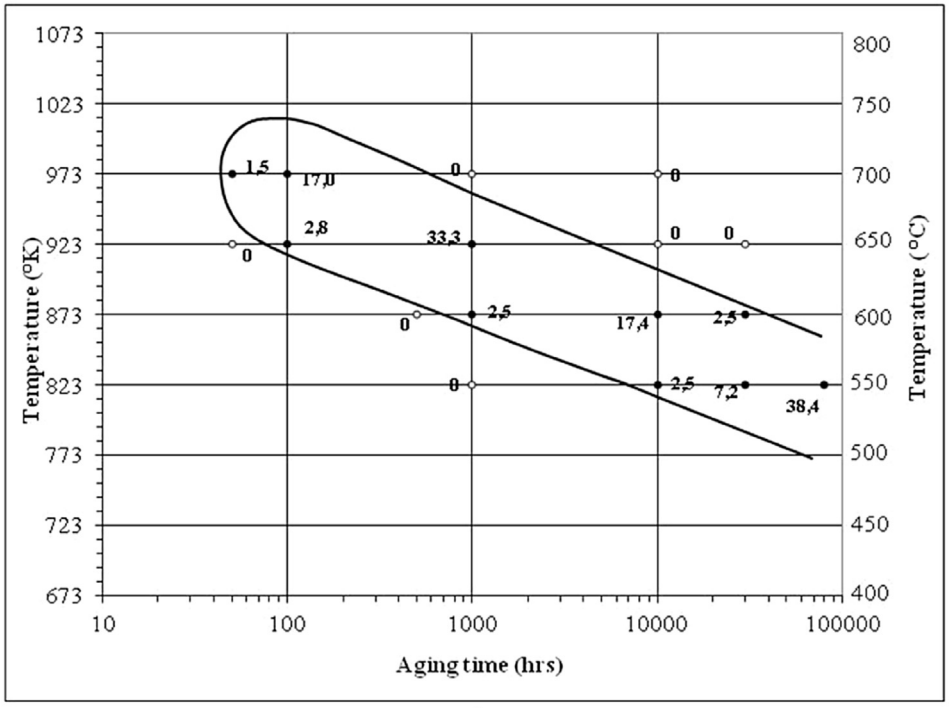

a

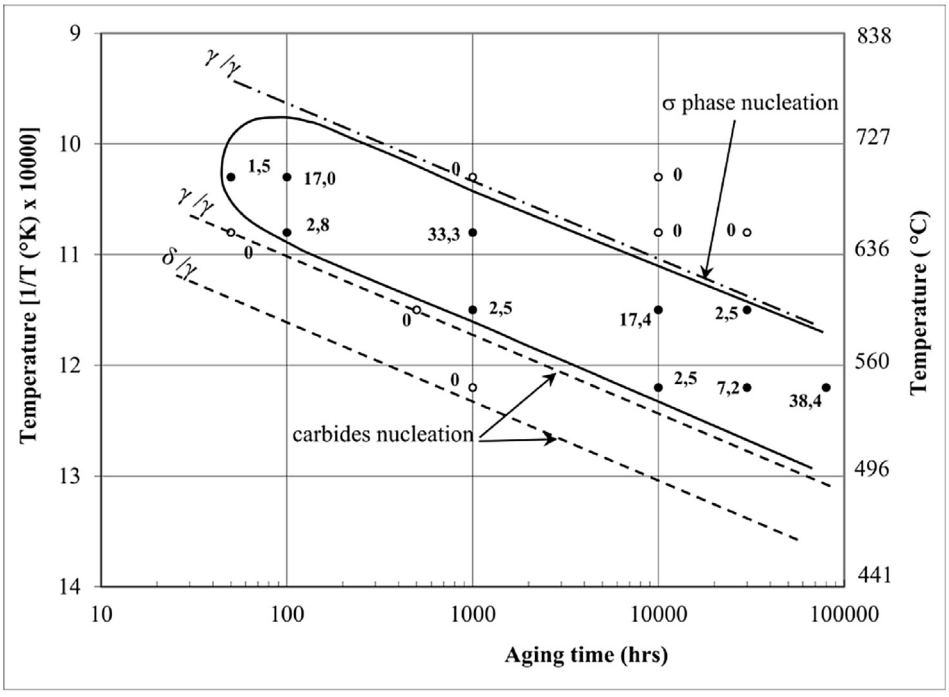

b

Fig. 12. Effect of rich-chromium phase on the IGC sensitization of AISI 316 L; (a) TTS diagram using the DOS resulting from DL-EPR tests; (b) Correlation between TTP and TTS.

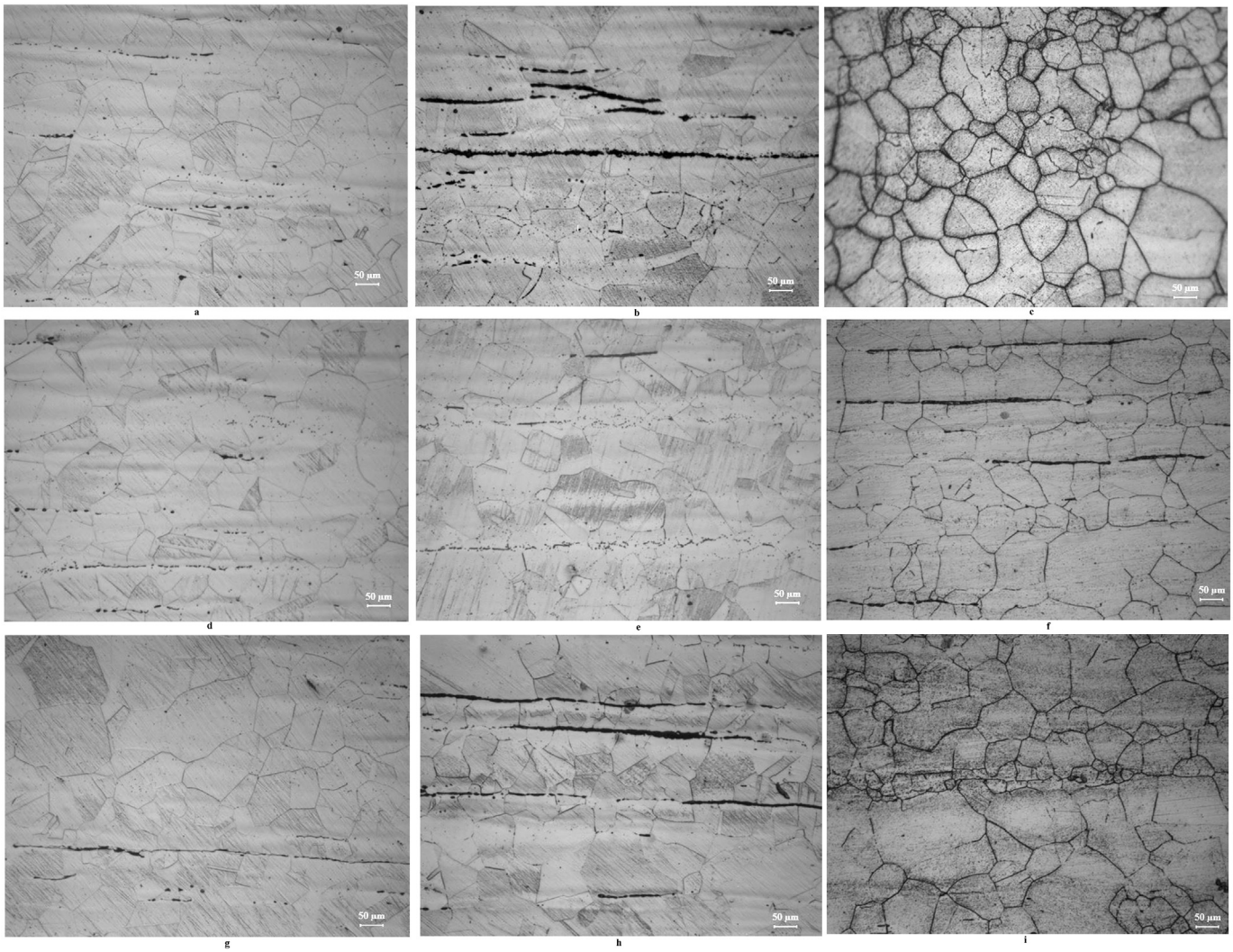

Fig. 13. ICG morphologies observed after the DL-EPR test (Optical micrographs); (a) 550 °C - 1000 h, DOS = 0%, step; (b) 550 °C - 10 000 h, DOS = 2.5%, dual; (c) 550 °C - 80 000 h, DOS = 38.4%, ditch; (d) 600 °C - 500 h, DOS = 0%, step; (e) 600 °C - 1000 h, DOS = 2.5%, dual; (f) 600 °C - 10 000 h, DOS = 17.4%, ditch, (g) 650 °C - 50 h, DOS = 0%, step; (h) 650 °C - 100 h, DOS = 2.8%, dual; (i) 650 °C - 1000 h, DOS = 33,3%, ditch.

which are characteristics of the corrosion behavior of low ferrite content AISI 316L stainless steel. It appears that aging at temperatures ranging from 550 to 700 °C for exposure periods varying between 100 h and 80 000 h generated various chromium-rich phases and mainly $M_{23}C_6$ which are responsible for chromium depletion in the vicinity of austenite grain boundaries and inside the ferrite islands. The nucleation and growth of carbides during aging modify significantly the size and the chromium concentration (% Cr) of the depleted areas as shown in column 3, 4 and 5 of Table 5. Columns 6 and 7 showed that the IGC sensitization corresponding to DOS $\geq$1% results in predominant intergranular attacks (ditch structure) occurring in the chromium-reduced areas with a concentration below the critical value of $(\%\,Cr)_{min} \leq$ 12-13 % wt and with a width more than 100 nm. Nevertheless, the desensitization, (self-healing) corresponding to a step structure, was achieved when the critical value of the chromium was recovered. The aged δ-ferrite islands are not significantly attacked since their chromium content remained above the critical value (12—13 %wt) during aging for short periods such as 1000 h at 550 °C, less than 100 h at 600 °C and 10 h at 650 °C. This concentration became higher ($\geq$14 %wt) after the total decomposition into chromium-rich secondary austenite (γ_r) and σ-phase which occurred for the long durations such as 30 000 h at 600 °C, more than 1000 h at 650 °C and 100 h at 700 °C.

5. Discussion

The weldability improvement of austenitic stainless steels requires a small fraction of δ-ferrite that could be achieved by rebalancing the austenitic stainless steel's chemical composition combined with annealing treatment conditions. Therefore, by controlling the equivalent chromium (Creq = 23.48 wt %) and the equivalent nickel (Nieq = 14.33 wt %) contents, the annealed AISI 316L structure consists of a small fraction of δ-ferrite dispersed in an austenite matrix. The subsequent thermo-mechanical treatments formed aligned islands of ferrite in the sheet's rolling direction. The Feritoscope FMP30 measurements provide a fraction of δ-ferrite of about 1% which is in agreement with values deduced from the Price & Andrews diagram [50].

Microstructural investigations, conducted in this study, confirmed the well-known instability of both γ-austenite and δ-ferrite components of the annealed structure during aging at temperatures ranging from 550 to 700 °C [27,46]. Moreover, the fast decomposition of δ-ferrite during aging is expected in accordance

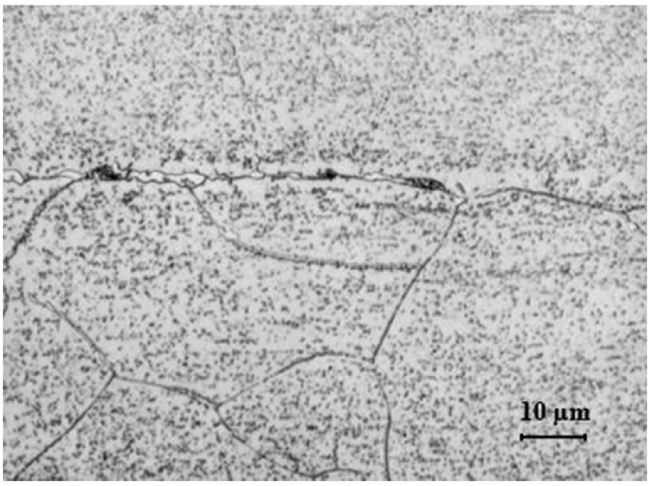

Fig. 14. Pits resulting from δ-ferrite decomposition observed in the vicinity of σ-phase after aging at 650 °C during 10 000 h.

with the literature results that attributed this phenomenon to the high chromium (27 wt %) and molybdenum (4 wt%) contents, compared to those of austenite which are equal to 17.3 wt % and 2.6 wt % respectively. Furthermore, the fast chromium diffusion in bcc structure of δ-ferrite comparatively to fcc structure of γ-austenite as reported in the literature [14] supports the TTP diagram results shown in Fig. 8, indicating the beginning of the chromium carbide precipitation at δ/γ interfaces during aging at temperature ranging from 550 to 700 °C. Therefore, the δ-ferrite decomposed gradually into chromium-rich $M_{23}C_6$ carbide and into chromium-rich and molybdenum intermetallic phases such as F.K, η, σ, χ and R. The ultimate stage of decomposition to σ-phase and regenerated austenite γ_r was achieved during aging at 650 °C and at 700 °C as shown in Fig. 7. These findings are complemented by the quantitative data reported in Table 2. The decomposition products of the δ-ferrite during aging have been reported in previous studies related to austenitic stainless steels with low ferrite content [27,31,34,46,51] and to duplex stainless steels [42,52]. This decomposition depends mainly on the chemical composition of the material and on aging temperature. In this study, it has been shown that the precipitation of staking faulted FK phase at the δ/γ interfaces was prior to that of $M_{23}C_6$ carbide due to the high concentration of chromium and molybdenum in δ-ferrite. By prolonging the aging period, the FK phase growth reduces the ferrite domain and consequently increases the carbon activity in the δ-ferrite that enhances the $M_{23}C_6$ carbide nucleation as shown in Fig. 4. In its turn, the growth of carbide consumes more chromium and molybdenum that favors the dissolution of metastable FK phase in benefit of more stable $M_{23}C_6$ carbide as shown in Figs. 5a and 6a. These findings are in accordance with the author's previous work [14,48]. The involved process of carbide growth is attributed to the diffusion of carbon atoms from γ-austenite and the diffusion of chromium and molybdenum atoms from δ-ferrite to the δ/γ interfaces as reported by several authors [14]. This process created chromium and molybdenum depleted zones inside the δ-ferrite reducing its chromium concentration from 27 wt % to 7 wt % during aging for very long duration at 550 °C as shown in Fig. 11. The chromium-depleted zone was also generated by intergranular γ/γ carbide and chromium concentration in the vicinity of grain boundaries and which continues to decrease as the growth process of carbide continues to operate. The replenishment occurs when the chromium-consuming process is slowed sufficiently due to the decrease of the carbon activity in the austenite. The dechromisation and rechromisation phenomena were illustrated by the chromium profiles shown in Fig. 10. Aging at higher temperatures accelerates the nucleation and the growth of carbides at the γ/γ grain boundaries and at the δ/γ interface, resulting in a significant decrease of the carbon content of austenite. Therefore, the chromium-rich and molybdenum-rich intermetallic phases, such as σ, χ and R, and requiring higher energy sites as reported in previous works [14,48], precipitate at the $M_{23}C_6/\gamma$ and $M_{23}C_6/\delta$ interfaces as shown in Fig. 7a. Laves phase η was also observed at the $M_{23}C_6/\gamma$ interface. It also exists within austenite grains through prolonging the aging period at 650 °C. The growth of these phases was likely to be performed at the expense of intergranular carbides which become less apparent compared to larger plates of σ-phase. However, the chromium depletion related to carbides is more significant than that resulting from intermetallic phases although they are also chromium-rich phases. Sahlaoui et al. [53] have demonstrated that nucleation of σ-phase required high energy sites and a chromium level higher than 14 wt%. The correlation between microstructure and the DOS, coupled with attack morphologies as in accordance with the ASTM A262 practice A standard, revealed that the IGC sensitization-desensitization are only controlled by the level and the extent of chromium depletion resulting from the nucleation and the growth of $M_{23}C_6$ carbide at the austenite grain

Table 5
Correlation between chromium depleted zones and IGC sensitization evaluated by the DOS values and IGC morphologies.

Aging conditions		Depleted zones characteristics			IGC Morphology	DOS (%) Resulting from DL-EPR tests
		Chromium level (wt. %)		Extend of depleted zone (nm)		
Temperature (°C)	Duration (h)	γ/γ	δ	W_D		
Annealed state		17.4	27	0	Step	0
550	1000	17.4	17.5	–	Step	0
	10 000	11	8.1	42	Dual	2.5
	30 000	10.5	8.8	110	Ditch	7.2
	80 000	12	10	215	Ditch	38.4
600	500	13	13	–	Step	0
	1000	11.8	7.7	72	Dual	2.5
	10 000	12.8	9	103	Ditch	17.4
	30 000	13.2	14[a]	0	Ditch	2.5
650	100	14	10	0	Dual	2.8
	1000	12.1	13.4	104	Ditch	33
	10 000	16.5	16[a]	0	Step	0
700	100	11.8	16[a]	–	Ditch	17

[a] Chromium level of regenerated austenite (γ_r) resulting from total decomposition of δ ferrite during aging.

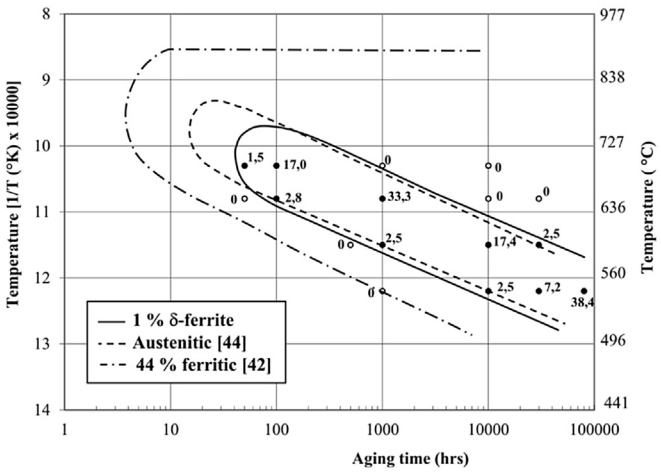

Fig. 15. Effect of ferrite content on the IGC sensitization of stainless steel derived from DL-EPR.

boundaries. It has been established that chromium depletion in the vicinity of austenite grain boundaries, below 12–13 wt% and extending over 100 nm in width sensitizes the AISI 316L with l % of δ-ferrite. However, the replenishment over 12–13 wt% of chromium leads to self-healing. Otherwise, the contribution of δ-ferrite to IGC sensitization seems to be not effective or negligible. This result corroborates Guanshun et al.'s one [46], indicating that the DOS of Ti modified Super 304H is still insignificant during aging at 650 °C for a δ-ferrite content below 3.9%. Increasing the ferrite fraction to 6.1% strongly deteriorates the IGC resistance at the same aging conditions. Authors attributed this result to the small contribution to IGC sensitization of the limited depleted areas related to low fraction of δ-ferrite. This tendency is clearly evidenced by Fig. 15, showing the superimposition of TTS curves corresponding to 0% [44] 1% (this study) and 45% [42] of δ-ferrite. Concerning this study, the correlation between microstructure and the DOS values provides more explanation. Indeed, after aging at 550 °C for relatively short period of up to 1000 h, the dechromisation into δ-ferrite was not enough (Cr ≥ 13 wt %) to provoke IGC, and therefore, the DOS remained less than 1%. By prolonging aging at the same temperature to up to 10 000 h, the DOS was higher than 2% and the "ditch" structure was related to chromium-depleted austenitic grain boundaries as shown in Fig. 13. This means that the contribution of the low fraction of chromium-depleted areas related to δ-ferrite and to DL-EPR response is negligible compared to that of the austenite grain boundaries areas. At higher temperatures, the δ-ferrite totally disappears with the associated depleted zones, since the chromium content of the regenerated austenite γ_r (Cr % = 16) is approximately equal to that of the initial γ-austenite (Cr % = 17.4). Therefore, the IGC sensitization is exclusively controlled by the chromium-depleted zones related to austenitic structure. That is why the TTS diagram of fully austenitic stainless steel completely coincides with that of low ferrite content austenitic stainless steel at very long aging durations, as shown in Fig. 15. In addition, chromium carbide ($M_{23}C_6$) and the associated chromium-depleted zones near the γ/γ grain boundaries are considered as the main element responsible for IGC sensitization of AISI 316L with 1% δ-ferrite since σ-phase appears at aging durations longer than 10 000 h at temperatures higher than 650 °C. These last parameters correspond to the occurrence of the rechromisation process which is in accordance with previous modeling and experimental work devoted to fully austenitic stainless steels [54]. Using TTS diagrams and equation (1) [13], the CCR to prevent IGC sensitization of AISI 316L with 1% δ-ferrite (24 K/h) has been determined and compared to that of AISI 316L fully austenitic stainless steel (86 K/h). The lower value of CCR corresponding to AISI 316L with 1% δ-ferrite is rather assigned as a beneficial effect of higher nitrogen level (N = 0.08 %wt) when compared to that of AISI 316L (N = 0.035 %wt), as reported by previous works [11–13].

6. Conclusion

Aging at temperatures ranging between 550 and 700 °C for periods varying from 50 h to 80 000 h modifies the microstructure and the IGC behavior of austenitic stainless steel AISI 316L with 1% δ-ferrite. The microstructural changes occur faster in ferrite than in austenite. The TTP diagram, constructed on the basis of TEM examination, outlines that precipitation processes are thermally active and controlled by chromium diffusion mechanism. The precipitation of chromium-rich and molybdenum-rich phases such as $M_{23}C_6$ carbide FK, η, σ, χ and R, generates a chromium-depleted area in ferrite and in the vicinity of austenite grain boundaries. However, the corrosion behavior of aged steel, assessed by DL-EPR tests, is only affected by the γ/γ $M_{23}C_6$ carbide precipitation and the associated chromium depletion zones. IGC sensitization occurred, in the conditions of this study, for DOS ≥1% when the chromium concentration falls below the critical value of 13 wt % and a width of the depleted zone higher than 100 nm. The self-healing is achieved when the critical value of chromium is recovered. The low ferrite content, recommended for hot cracking resistance and its decomposition products such as σ, χ and R during aging, does not alter the steel corrosion behavior since the TTS diagram remained coincident with that of fully austenitic stainless steel. The CCR preventing any risk of IGC sensitization, and calculated from the TTS diagram and using Dayal method, is found to be 24 K/h.

References

[1] M. Cindra Fonseca, I.N. Bastos, E. Baggio-Saitovitch, D.R. Sánchez, Characterization of oxides of stainless steel UNS S30400 formed in offshore environment, Corros. Sci. 55 (2012) 34–39.

[2] C. Jullien, T. Bénézech, B. Carpentier, V. Lebret, C. Faille, Identification of surface characteristics relevant to the hygienic status of stainless steel for the food industry, J. Food Eng. 56 (2003) 77–87.

[3] Y. Ke, R. Yibin, Nickel-free austenitic stainless steels for medical applications, Sci. Technol. Adv. Mater. 11 (2010) 014105.

[4] M. Talha, C.K. Behera, O.P. Sinha, A review on nickel-free nitrogen containing austenitic stainless steels for biomedical applications, Mater. Sci. Eng. C 33 (2013) 3563–3575.

[5] E. Mohammadi Zahrani, A. Saatchi, A. Alfantazi, Pitting of 316L stainless steel in flare piping of a petrochemical plant, Eng. Fail. Anal. 17 (2010) 810–817.

[6] M. Milititsky, D.K. Matlock, A. Regully, N. Dewispelaere, J. Penning, H. Hanninen, Impact toughness properties of nickel-free austenitic stainless steels, Mater. Sci. Eng. A 496 (2008) 189–199.

[7] H. Sidhom, A. Ben Rhouma, C. Braham, J. Ledion, Préparation des surfaces et tenue à la corrosion localisée des aciers inoxydables austénitiques, Matér. Tech. 86 (N° 9–10) (1998) 31–37.

[8] A.B. Rhouma, H. Sidhom, C. Braham, J. Lédion, M.E. Fitzpatrick, Effects of surface preparation on pitting resistance, residual stress, and stress corrosion cracking in austenitic stainless steels, J. Mater. Eng. Perform. 10 (2001) 507–514.

[9] G. Bai, S. Lu, D. Li, Y. Li, Influences of niobium and solution treatment temperature on pitting corrosion behaviour of stabilised austenitic stainless steels, Corros. Sci. 108 (2016) 111–124.

[10] B. Kartik, R. Veerababu, M. Sundararaman, D.V.V. Satyanarayana, Effect of high temperature ageing on microstructure and mechanical properties of a nickel-free high nitrogen austenitic stainless steel, Mater. Sci. Eng. A 642 (2015) 288–296.

[11] Y.J. Oh, J.H. Hong, Nitrogen effect on precipitation and sensitization in cold-worked Type 316L(N) stainless steels, J. Nucl. Mater. 278 (2000) 242–250.

[12] R. Beneke, R.F. Sandenbergh, The influence of nitrogen and molybdenum on the sensitization properties of low-carbon austenitic stainless steels, Corros. Sci. 29 (1989) 543–555.

[13] N. Parvathavarthini, R.K. Dayal, Time–temperature-sensitization diagrams and critical cooling rates of different nitrogen containing austenitic stainless steels, J. Nucl. Mater. 399 (2010) 62–67.

[14] H. Sidhom, Etude de l'évolution structural au cours du vieillissement de deux aciers inoxydables austénitiques, et de son influence sur les propriétés

mécaniques et la corrosion inter-cristalline, University of Paris XI, Paris, 1990.
[15] A. Pardo, M.C. Merino, A.E. Coy, F. Viejo, M. Carboneras, R. Arrabal, Influence of Ti, C and N concentration on the intergranular corrosion behaviour of AISI 316Ti and 321 stainless steels, Acta Mater. 55 (2007) 2239–2251.
[16] K. Chandra, V. Kain, R. Tewari, Microstructural and electrochemical characterisation of heat-treated 347 stainless steel with different phases, Corros. Sci. 67 (2013) 118–129.
[17] H.S.I. Trigui, C. Braham, J. Lédion, La corrosion par piqûres d'aciers inoxydables austéno-ferritiques dans l'eau de mer synthétique - influence de la composition chimique et de la teneur inclusionnaire, matériaux et techniques, Hors séris, 1996, pp. 23–30.
[18] J. Verma, R.V. Taiwade, Dissimilar welding behavior of 22% Cr series stainless steel with 316L and its corrosion resistance in modified aggressive environment, J. Manuf. Process. 24 (Part 1) (2016) 1–10.
[19] M. Ziętala, T. Durejko, M. Polański, I. Kunce, T. Płociński, W. Zieliński, M. Łazińska, W. Stępniowski, T. Czujko, K.J. Kurzydłowski, Z. Bojar, The microstructure, mechanical properties and corrosion resistance of 316 L stainless steel fabricated using laser engineered net shaping, Mater. Sci. Eng. A 677 (2016) 1–10.
[20] Y. Cai, Z. Luo, M. Feng, Z. Liu, Z. Huang, Y. Zeng, Effect of activator on mechanical properties and intercrystalline corrosion resistance of austenitic stainless steel weld, J. Mater. Process. Technol. 234 (2016) 243–248.
[21] C. Garcia, F. Martin, P. de Tiedra, Y. Blanco, M. Lopez, Pitting corrosion of welded joints of austenitic stainless steels studied by using an electrochemical minicell, Corros. Sci. 50 (2008) 1184–1194.
[22] M. Dadfar, M.H. Fathi, F. Karimzadeh, M.R. Dadfar, A. Saatchi, Effect of TIG welding on corrosion behavior of 316L stainless steel, Mater. Lett. 61 (2007) 2343–2346.
[23] C. Braham, A. Ben Rhouma, J. Lédion, H. Sidhom, Effect of machining conditions on residual stress corrosion cracking of 316L SS, Mater. Sci. Forum 490–491 (2005) 305–310.
[24] J.B. Cai, C. Yu, R.K. Shiue, L.W. Tsay, Stress corrosion cracking of austenitic weld deposits in a salt spray environment, J. Nucl. Mater. 465 (2015) 774–783.
[25] K.N. Lyon, T.J. Marrow, S.B. Lyon, Influence of milling on the development of stress corrosion cracks in austenitic stainless steel, J. Mater. Process. Technol. 218 (2015) 32–37.
[26] J.Z. Lu, K.Y. Luo, D.K. Yang, X.N. Cheng, J.L. Hu, F.Z. Dai, H. Qi, L. Zhang, J.S. Zhong, Q.W. Wang, Y.K. Zhang, Effects of laser peening on stress corrosion cracking (SCC) of ANSI 304 austenitic stainless steel, Corros. Sci. 60 (2012) 145–152.
[27] A.Y. Kina, V.M. Souza, S.S.M. Tavares, J.M. Pardal, J.A. Souza, Microstructure and intergranular corrosion resistance evaluation of AISI 304 steel for high temperature service, Mater. Charact. 59 (2008) 651–655.
[28] A. Abou-Elazm, R. Abdel-Karim, I. Elmahallawi, R. Rashad, Correlation between the degree of sensitization and stress corrosion cracking susceptibility of type 304H stainless steel, Corros. Sci. 51 (2009) 203–208.
[29] M. Matula, L. Hyspecka, M. Svoboda, V. Vodarek, C. Dagbert, J. Galland, Z. Stonawska, L. Tuma, Intergranular corrosion of AISI 316L steel, Mater. Charact. 46 (2001) 203–210.
[30] M. Terada, D.M. Escriba, I. Costa, E. Materna-Morris, A.F. Padilha, Investigation on the intergranular corrosion resistance of the AISI 316L(N) stainless steel after long time creep testing at 600 °C, Mater. Charact. 59 (2008) 663–668.
[31] N. Yoshikuni, N. Kazutoshi, I. Mitsunori, Influence of delta-ferrite on sensitization of the austenitic stainless steel weld metal, Q. J. Jpn. Weld. Soc. 9 (1991) 415–422.
[32] F. Wilson, Mechanism of intergranular corrosion of austenitic stainless steels—literature review, Br. Corros. J. 6 (1971) 100–108.
[33] J.J. Heger, J.L. Hamilton, Effect of minor constituents on the intergranular corrosion of austenitic stainless steels, Corrosion 11 (1) (1955) 22–26.
[34] T. Ogawa, E. Tsunetomi, Hot cracking susceptibility of austenitic stainless steels, Weld. Res. Suppl. 61 (1982) 82s–93s.
[35] J.C. Lippold, W.F. Savage, Characterization of weld solidification cracking in a duplex stainless steel weldments: Part III—the effect of solidification behavior on hot cracking susceptibility, Weld. Res. Suppl. 61 (1982) 88S–96S.
[36] P. Manning, D. Duquette, W. Savage, Technical Note: the effect of retained ferrite on localized corrosion in duplex 304L stainless steel, Weld. J. (1980) 260–262.
[37] C.L. Lai, L.W. Tsay, W. Kai, C. Chen, The effects of cold rolling and sensitisation on hydrogen embrittlement of AISI 304L welds, Corros. Sci. 52 (2010) 1187–1193.
[38] ASTM A262-10, Standard Practices for Detecting Susceptibility to Intergranular Attack in Austenitic Stainless Steels, New York, 2010.
[39] Report No. NF EN ISO 3651–2, AFNOR, Cedex, France, 1998.
[40] Report No. NF EN ISO 3651–1, AFNOR, Cedex, France, 1998.
[41] ASTM A262–02a (Reapproved 2008), Standard Practices for Detecting Susceptibility to Intergranular Attack in Austenitic Stainless Steels, ASTM, PA, 2008.
[42] T. Amadou, H. Sidhom, C. Braham, Double loop electrochemical potentiokinetic reactivation test optimization in checking of duplex stainless steel intergranular corrosion susceptibility, Metall. Mater. Trans. A 35 (2004) 3499–3513.
[43] H. Sidhom, T. Amadou, C. Braham, Evaluation by the double loop electrochemical potentiokinetic reactivation test of aged ferritic stainless steel intergranular corrosion susceptibility, Metall. Mater. Trans. A 41 (2010) 3136–3150.
[44] H. Sidhom, T. Amadou, H. Sahlaoui, C. Braham, Quantitative evaluation of Aged AISI 316L stainless steel sensitization to intergranular corrosion: comparison between microstructural electrochemical and analytical methods, Metall. Mater. Trans. A 38 (2007) 1269–1280.
[45] G.H. Aydoğdu, M.K. Aydinol, Determination of susceptibility to intergranular corrosion and electrochemical reactivation behaviour of AISI 316L type stainless steel, Corros. Sci. 48 (2006) 3565–3583.
[46] G. Bai, S. Lu, D. Li, Y. Li, Intergranular corrosion behavior associated with delta-ferrite transformation of Ti-modified Super304H austenitic stainless steel, Corros. Sci. 90 (2015) 347–358.
[47] C. Garcia, M.P. de Tiedra, Y. Blanco, O. Martin, F. Martin, Intergranular corrosion of welded joints of austenitic stainless steels studied by using an electrochemical minicell, Corros. Sci. 50 (2008) 2390–2397.
[48] H. Sidhom, R. Portier, An icosahedral phase in annealed austenitic stainless steel? Philos. Mag. Lett. 59 (1989) 131–139.
[49] D. Carron, P. Chemelle, D. Michel, M.J. Hytch, R. Portier, Icosahedral related precipitation at a nanometric scale in a superferritic steel, J. Non Cryst. Solids 153–154 (1993) 473–477.
[50] K.W.A.L. Pryce, Practical estimation of composition balance and ferrite content in stainless steels, Iron Steel Inst. 195 (1960) 415–417.
[51] W. Jolly, C. Toffolon-Masclet, J.M. Joubert, B. Marini, F. Porcher, G. André, F. Cortial, P. Petit, S. Ringeval, In situ monitoring of isothermal phase transformation in two Nb stabilized austenitic stainless steels (316Nb) by neutron diffraction, J. Alloys Compd. 688 (Part B) (2016) 695–702.
[52] S.-M. Yang, Y.-C. Chen, C.-H. Chen, W.-P. Huang, D.-Y. Lin, Microstructural characterization of δ/γ/σ/γ2/χ phases in silver-doped 2205 duplex stainless steel under 800 °C aging, J. Alloys Compd. 633 (2015) 48–53.
[53] H. Sahlaoui, H. Sidhom, Experimental investigation and analytical prediction of σ-phase precipitation in AISI 316L austenitic stainless steel, Metall. Mater. Trans. A 44 (2013) 3077–3083.
[54] H. Sahlaoui, K. Makhlouf, H. Sidhom, J. Philibert, Effects of ageing conditions on the precipitates evolution, chromium depletion and intergranular corrosion susceptibility of AISI 316L: experimental and modeling results, Mater. Sci. Eng. A 372 (2004) 98–108.